

Extension of the modified Mohr-Coulomb fracture model by a strain rate and temperature dependence

VASQUEZ RAMIREZ Dominyka^{1,a *}, WESTER Hendrik^{1,b},
ROSENBUSCH Daniel^{1,c} and BEHRENS Bernd-Arno^{1,d}

¹Gottfried Wilhelm Leibniz Universität, Institute of Forming Technology and Machines, An der Universität 2, 30823 Garbsen, Germany

^avasquezramirez@ifum.uni-hannover.de, ^bwester@ifum.uni-hannover.de,

^crosenbusch@ifum.uni-hannover.de, ^dbehrens@ifum.uni-hannover.de

Keywords: Fracture Characterisation, MMC Fracture Model, Dual-Phase Steel

Abstract. During industrial sheet metal processes such as shear cutting, high temperatures and strain rates occur. Due to materials dependency on temperature and strain rate, the numerical fracture modelling should consider these both highly influential factors for accurate simulation results. Since the widely used Modified Mohr-Coulomb (MMC) fracture model does not take the dependency on temperature and strain rate into account, the objective of this research is therefore to extend the MMC fracture model. For the fracture characterization, miniaturised tensile tests under variation of specimen geometry, temperature and strain rate are conducted. Additionally, tensile tests with butterfly specimens under varying stress states are carried out. In order to determine material specific MMC parameters, the experimental tests are numerically depicted in Abaqus. The temperature and strain rate extension of the MMC fracture model is based on the Johnson-Cook failure model. With this approach, a temperature and strain-rate dependent MMC fracture model is developed for the dual phase steel DP980.

Introduction

Any sheet metal procedure, whether it is cutting or forming, begins with a suitable process design to describe materials forming behaviour under specific process conditions [1]. A cost- and time-efficient possibility for such investigations is the Finite Element (FE) method, which is built upon a specific material model [2]. Based on a thorough material investigation, it is possible to predict material fracture depending on stress or strain in a specific process using FE [3]. This research therefore covers an extension of a fracture model regarding temperature and strain rate on a DP980 sheet metal. For this purpose, Modified Mohr-Coulomb (MMC) fracture model was extended with Johnson-Cook (J-C) [4] strain rate hardening and thermal softening effect terms using experimental results from various tensile tests that cover a specific stress, temperature and strain rate field.

The Mohr-Coulomb (MC) fracture model combines the normal stresses σ_1 , σ_2 and σ_3 to calculate material failure in dependence on friction coefficient c_1 and shear resistance c_2 [5]:

$$c_2 = \max \left\{ \frac{1}{2} |\sigma_1 - \sigma_2| + c_1 (\sigma_1 + \sigma_2), \frac{1}{2} |\sigma_2 - \sigma_3| + c_1 (\sigma_2 + \sigma_3), \frac{1}{2} |\sigma_3 - \sigma_1| + c_1 (\sigma_3 + \sigma_1) \right\} \quad (1)$$

In [5] it was also shown that the normal stresses can be given as a function of mean stress σ_m , stress triaxiality η and normalised Lode angle $\bar{\theta}$. Subsequently, the MC model can be represented as a function of the equivalent stress $\bar{\sigma}$, η and $\bar{\theta}$. However, the model only describes failure in a stress based space, which is not accurate when modelling materials fracture. Nonetheless, the transformation of the equation from a solely stress based into a stress and strain based space under condition of monotonic loading allowed to define the MMC failure model in terms of equivalent plastic strain at fracture $\bar{\epsilon}_p^f$ [6]. Therefore, with A and n as strength and work hardening exponents



of the Swift hardening law, respectively, as well as c_3 as a material constant, the MMC failure model is defined as follows [7]:

$$\bar{\varepsilon}_p^f = \left\{ \frac{A}{c_2} \left[c_3 + \frac{\sqrt{3}}{2-\sqrt{3}} (1 - c_3) \left(\sec\left(\frac{\bar{\theta}\pi}{6}\right) - 1 \right) \right] \left[\sqrt{\frac{1+c_1^2}{3}} \cos\left(\frac{\bar{\theta}\pi}{6}\right) + c_1 \left(\eta + \frac{1}{3} \sin\left(\frac{\bar{\theta}\pi}{6}\right) \right) \right] \right\}^{-\frac{1}{n}} \quad (2)$$

However, the MMC fracture model does not directly take the temperature nor the strain rate into account. In [6] it was shown, that DP980 changes its characteristics when exposed to higher temperatures. For this reason, in [6] it was investigated whether the temperature influence reflects on the MMC fracture model. As a result, it was depicted that the MMC fracture model and its parameters are highly dependent on materials behaviour under increasing temperatures. Another investigation was conducted in [8] on a DP590 steel, where the strain rate influence on the Hosford-Coulomb fracture model was demonstrated. These examples conclude, that a varying material behaviour, influenced by temperature and strain rate, is an important factor when parametrising a fracture model and should therefore be taken into account for accurate modelling.

An exemplary solution was proposed in [9], where a failure model DF2014 was successfully extended using the strain rate hardening and thermal softening effect terms of the J-C failure model for a AA7075 sheet material. Similar approach is applied in this research as well by using the MMC fracture model as the basis with an extension by the strain rate and thermal effect terms of the J-C failure model to define the following equation:

$$\bar{\varepsilon}_p^f = \left\{ \frac{A}{c_2} \left[c_3 + \frac{\sqrt{3}}{2-\sqrt{3}} (1 - c_3) \left(\sec\left(\frac{\bar{\theta}\pi}{6}\right) - 1 \right) \right] \left[\sqrt{\frac{1+c_1^2}{3}} \cos\left(\frac{\bar{\theta}\pi}{6}\right) + c_1 \left(\eta + \frac{1}{3} \sin\left(\frac{\bar{\theta}\pi}{6}\right) \right) \right] \right\}^{-\frac{1}{n}} \cdot \left[1 + d_1 \left(\frac{T - T_{ref}}{T_{melt} - T_{ref}} \right) \right] \left[1 + d_2 \ln\left(\frac{\bar{\varepsilon}^{pl}}{\dot{\varepsilon}_0}\right) \right] \quad (3)$$

With d_1 and d_2 indicated as material parameters, T as current temperature, T_{ref} as reference temperature of 20°C, T_{melt} as melting point of the material at 1520°C [10], $\bar{\varepsilon}^{pl}$ as equivalent plastic strain and $\dot{\varepsilon}_0$ as reference strain rate at 0.001 1/s. For the determination of the individual temperature and strain rate dependent material parameters, such as plastic strain at fracture, normalised Lode angle and stress triaxiality, various material characterization tests and subsequent simulations with Abaqus are carried out, which are presented in the next chapters.

Experimental Tests

Miniaturised tensile tests. Miniaturised specimens of three different geometries were used to conduct isothermal tensile tests at various temperatures on a quenching and forming dilatometer DIL 805A/D+T. Additionally, an optical measurement system Aramis was applied to correctly indicate the length change at fracture by means of digital image correlation (DIC). The schematic setup of the dilatometer and its corresponding components is presented in [6]. A uniaxial and two notched specimen geometries with a radius of 3 and 10 mm were chosen as miniaturised tensile specimens, which are shown in Fig. 1 (a). Geometry variation during the miniaturised tensile tests served to induce different stress states on the material in order to cover various stress triaxiality and normalised Lode angle values. The tensile tests were conducted at temperatures between 20 and 600 °C, while the strain rate was held constant at 0.001 s⁻¹.

Tensile tests on butterfly specimens. The butterfly specimen, shown in Fig. 1 (b), was tested under different loading angles in an interval of 15.5°, as shown in Fig. 1 (c), thus varying the stress state from shear to uniaxial tension. Five loading angles were tested at 20°C with a constant forming speed of 0.001 1/s. The tests were conducted on a tensile testing machine S100/ZD with an optical measurement system Aramis to track the displacement in x and y direction. A stochastic pattern was applied on both miniaturised and butterfly tensile specimens for the DIC

measurements. A more detailed setup of the butterfly tensile testing equipment and its corresponding components is presented in [2] and [11].

High speed tensile tests. The high speed uniaxial tensile tests were conducted on a high speed tearing machine SZM500 with the specimen geometry shown in Fig. 1 (d). The deformation was recorded by means of a high speed camera and subsequently evaluated using greyscale correlation. Strain gauges were applied due to the expected high vibrations caused by the high strain rates. The testing temperature was held constant at 20 °C, whereas the strain rate varied between 100, 500 and 1000 1/s to cover a wide range of strain rates that occur in various sheet metal processes, e.g. in shear cutting. The sheet metal thickness of the DP980 material used was 1 mm for each test.

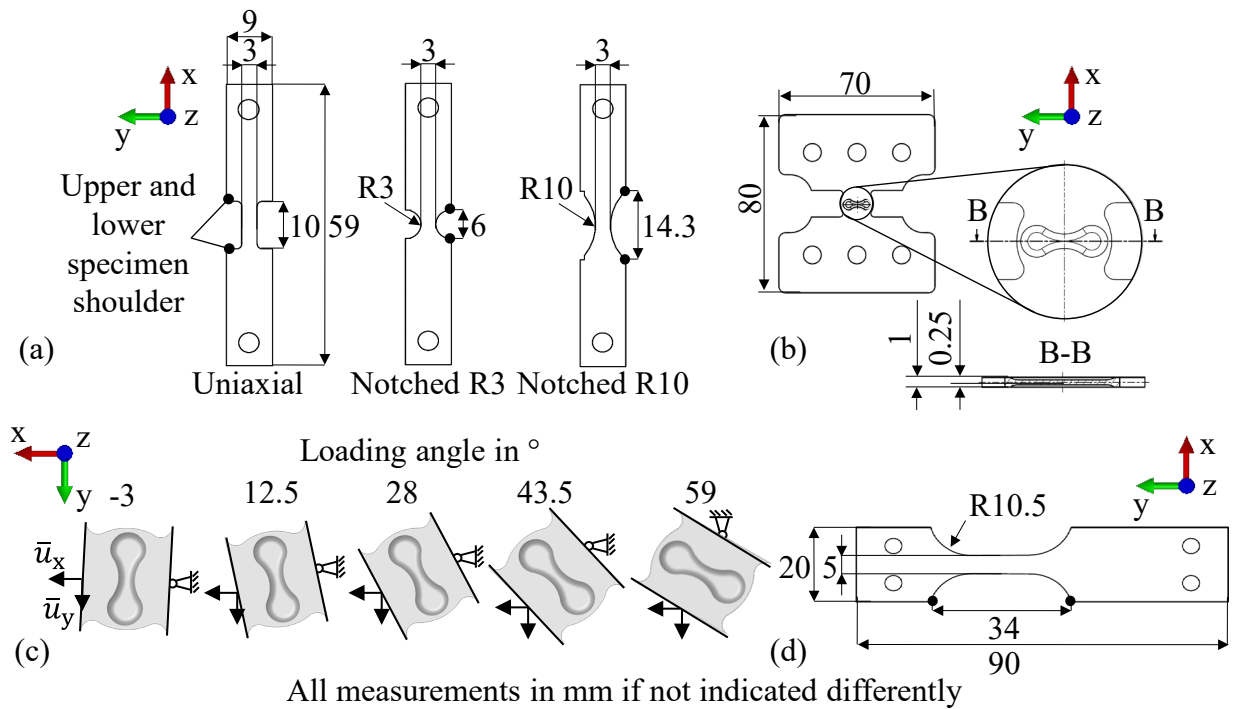


Fig. 1. Miniaturised tensile specimens (a), butterfly specimen (b), loading angles of butterfly tensile tests (c) and high speed tensile specimen (d).

Numerical Modelling

Each of the conducted experimental tests were simulated in Abaqus/implicit to determine the parameters of the extended MMC fracture model. For this purpose, temperature and strain rate dependent flow curves were modelled using uniaxial tensile test results of miniaturised and high speed specimens. Then, the acquired flow curves were extrapolated via a combined approach of Swift [12] and Voce [13] with k_{Comb} as flow stress, ε as plastic strain, ε_0 as starting plastic strain, σ_0 as yield stress, σ_s and E as material parameters and α as a weighting factor of 0.7, which was determined using the least squares method:

$$k_{Comb}(\varepsilon) = \alpha \cdot A(\varepsilon_0 + \varepsilon)^n + (1 - \alpha)(\sigma_s + (\sigma_0 - \sigma_s))e^{(-\frac{\varepsilon}{E})} \quad (4)$$

Anisotropic parameters, determined experimentally using miniaturised uniaxial tensile tests on specimens produced in 0°, 45° and 90° to rolling direction, were calculated using Hill'48 approach and implemented as R_{11} , R_{22} , R_{33} , R_{12} , R_{13} and R_{23} variables in the numerical calculation. Moreover, time-displacement curves of each experimental test were determined and applied as an amplitude input in the numerical simulation with the exception of the butterfly tests, where the time-displacement curves in x and y direction were used as displacement boundary condition. In

the numerical simulation of the experimental tests, one end of the specimen was always fixed, while the other was exposed under translatory motion according to the amplitude. During the simulation of the butterfly tests, fracture was indicated when the maximum displacement in x and y directions was reached. For the miniaturised and high speed tensile tests, the length change was measured between the upper and lower specimen shoulder, exemplary shown in Fig. 1 (a) and (d), until the length change at fracture from experiments was reached, thus indicating fracture.

Solid eight node elements type C3D8R were used for the simulations with an element edge length of 0.1 mm and an application of symmetries on miniaturised and high speed tensile specimens both in y and z directions. Symmetry in the z direction was used for butterfly tensile specimens. Direct method was applied as a solver with a full Newton solution technique. Equivalent plastic strain at fracture $\bar{\varepsilon}_p^f$, stress triaxiality η and normalised Lode angle $\bar{\theta}$ were determined for each simulated test. Since the stress state varied during the deformation, integral calculation of η and $\bar{\theta}$ over the plastic strain at fracture was carried out to determine the average stress triaxiality η_{av} and average normalised Lode angle $\bar{\theta}_{av}$ [7]:

$$\eta_{av} = \frac{1}{\bar{\varepsilon}_p^f} \int_0^{\bar{\varepsilon}_p^f} \eta(\varepsilon_p) d\varepsilon_p \quad \bar{\theta}_{av} = \frac{1}{\bar{\varepsilon}_p^f} \int_0^{\bar{\varepsilon}_p^f} \theta(\varepsilon_p) d\varepsilon_p \quad (5)$$

The aforementioned tensile simulations were conducted for each specimen geometry, temperature and strain rate to determine the parameters of the extended MMC fracture model, given in Eq. 3. For this reason, experimental tests at 20°C and 0.001 1/s with subsequent numerical results were used to determine parameters c_1 , c_2 and c_3 , shown in Eq. 2. Miniaturised and butterfly tensile test results were applied for this purpose. Subsequently, results from miniaturised tensile tests between 100 and 600°C at 0.001 1/s were used to determine material constant d_1 of the temperature extension term. A similar approach was applied to determine material constant d_2 of the strain rate extension term using miniaturised uniaxial and high speed tensile test results at 20 °C, which were conducted at strain rates between 0.001 and 1000 1/s. Parameters A , n , c_1 , c_2 and c_3 were held constant during the determination of d_1 and d_2 .

Results and Discussions

Tensile test results. Experimental test results from miniaturised uniaxial and high speed tensile tests are shown in Fig. 2 in form of extrapolated flow curves using the aforementioned approach in Eq. 4. Fig. 2 (a) shows flow curves at 0.001 1/s of the miniaturised uniaxial specimens at all considered temperatures, whereas Fig. 2 (b) illustrates flow curves at various strain rates of the uniaxial specimens at 20°C. An interesting phenomenon can be pointed out in Fig. 2 (a), which is the so called blue-brittleness [6]. It indicates, that at specific temperatures materials strength does not decrease with increasing temperature due to foreign atom diffusion at dislocations. Therefore, the flow curve behaviour between 20 and 300 °C barely deviates from each other. Starting at 400 °C, however, materials thermal softening overcomes the blue-brittleness effect, resulting in a strong decrease of flow stress with increasing temperature. The strain rate influence, shown in Fig. 2 (b), portrays an interesting behaviour as well in which the flow stress at 0.001 and 100 1/s as well as at 500 and 1000 1/s begins with a similar yield stress. However, with an increasing plastic strain, the flow curve at a higher strain rate overcomes the one at a lower strain rate. This is due to the logarithmic dependence of the yield stress on the strain rate, in which only small differences are observed regarding the yield stress within the quasi-static and medium strain rates of 0.001 and 100 1/s as well as between the dynamic strain rates of 500 and 1000 1/s [14]. The logarithmic strain rate dependence is therefore the reason for the yield stress leap between the strain rates of 0.001 - 100 1/s and 500 - 1000 1/s. Moreover, dual phase steels have been proven to have a low strain rate sensitivity in regard of yield stress [15]. The portrayed flow curves were implemented

in the numerical simulation of each tensile geometry for the corresponding temperature and strain rate, including the ones of the notched and butterfly tensile specimens.

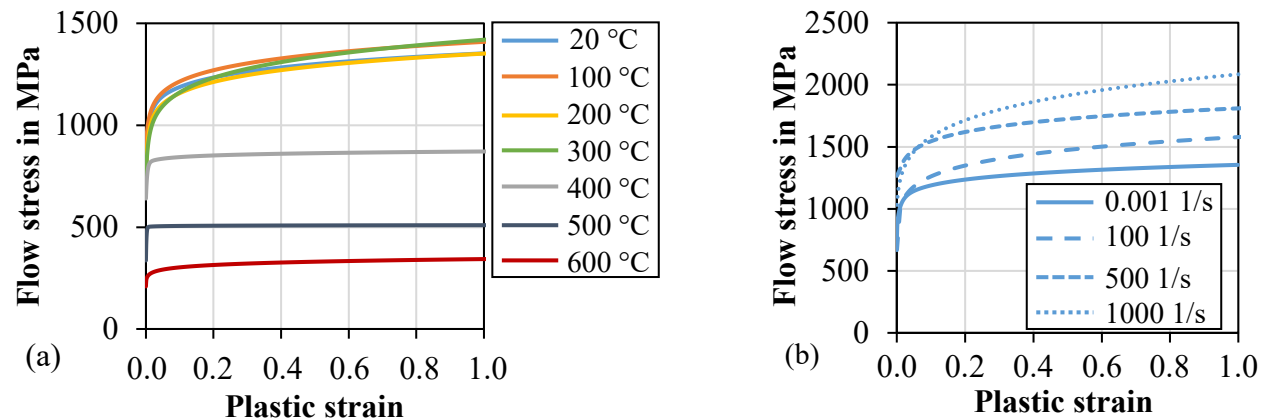


Fig. 2. Extrapolated flow curves of uniaxial tensile tests: at 0.001 1/s varying the forming temperature (a) and at 20 °C varying the strain rate (b).

Numerical results. Each numerically depicted tensile test was verified by comparing force-displacement curves with the experimentally determined results. This verification approach is exemplary shown in Fig. 3, illustrating a comparison of the numerically and experimentally determined force-displacement curves of the miniaturised uniaxial tensile tests for all temperatures at 0.001 1/s. For a better visualisation, the force-displacement curves are split into (a) and (b).

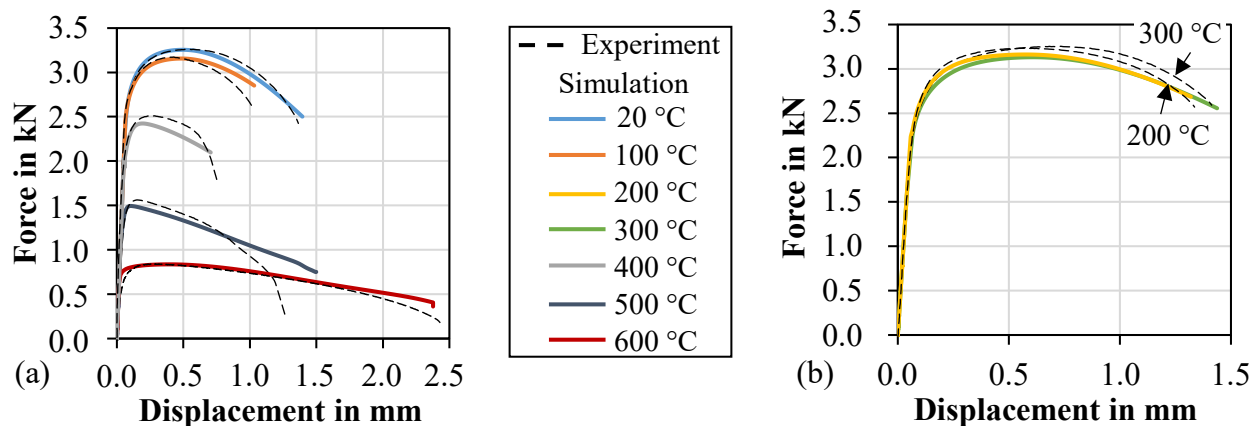


Fig. 3. Verification of numerically determined force-displacement curves with experimental results of miniaturised uniaxial tensile tests at 20, 100, 400 - 600 °C (a) and at 200 - 300 °C (b).

Overall, good agreement was observed. The force-displacement curves at 400 and 500 °C show the largest deviation between the numerical and experimental results, in particularly after reaching maximal tensile strength. This is due to the fact that no damage was taken into account when simulating the tensile tests. Damage consideration serves for a better depiction of material softening when localized necking occurs, since it takes the effect of decreased loading capacity caused by defect structure development into account [16]. Moreover, in Fig. 3 the blue-brittleness effect can be depicted once more, in particularly between 20 and 200 °C regarding both the maximal force and maximal displacement. The blue-brittleness effect was mainly observed in the miniaturised uniaxial specimens and not in the notched specimens.

Finally, the verified numerical results from each tensile test were used to determine the extended MMC fracture model parameters. Fig. 4 shows exemplary curves of plastic strain as a function of

stress triaxiality (a) and normalised Lode angle (b) for all tensile specimens at 20°C and 0.001 1/s. As mentioned in the introduction, stress triaxiality and normalised Lode angle change over the course of plastic strain, which is particularly visible on the miniaturised tensile specimens. For this reason, Eq. 5 is used to calculate the average values of η_{av} and $\bar{\theta}_{av}$. A stress triaxiality ranging from -0.1 to 0.99 and a normalised Lode angle between -0.04 and 0.5 were covered at 20°C and 0.001 1/s, while reaching a plastic strain of fracture up to 0.75.

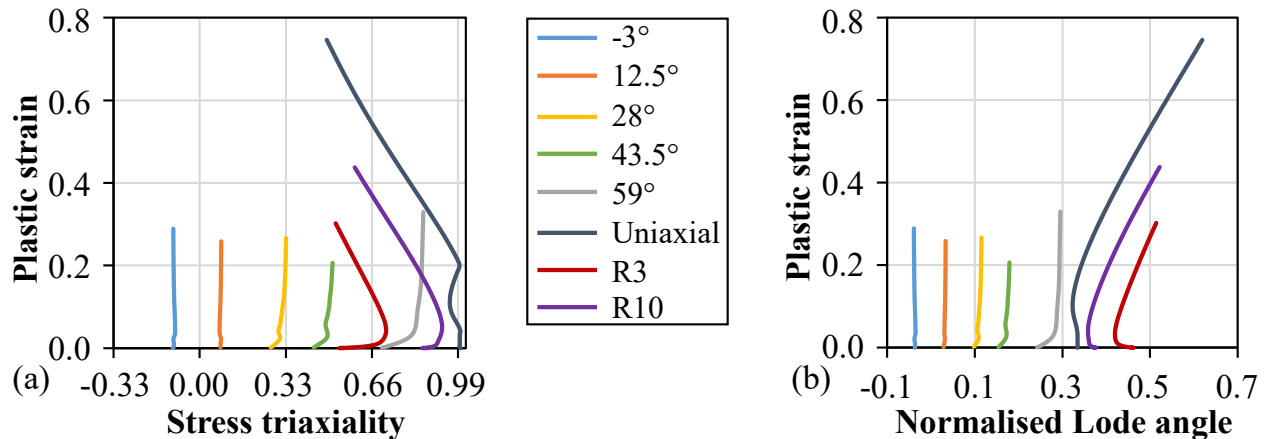


Fig. 4. Plastic strain over stress triaxiality (a) and plastic strain over normalised Lode angle (b) for all tensile specimens at 20°C and 0.001 1/s.

Fig. 5 (a) shows average normalised Lode angle over average stress triaxiality of the tested specimens between 20 and 600°C at 0.001 1/s. The black lines in Fig. 5 indicate the two-dimensional plane strain and plane stress states which occur in sheet metal forming. Fig. 5 (b) serves for a better illustration of η_{av} and $\bar{\theta}_{av}$ at a temperature field of 20 - 300°C. Here, blue-brittleness effect can be depicted again, in which the average values of stress triaxiality for uniaxial specimen are lower in the field of 100 - 300°C than at 20°C.

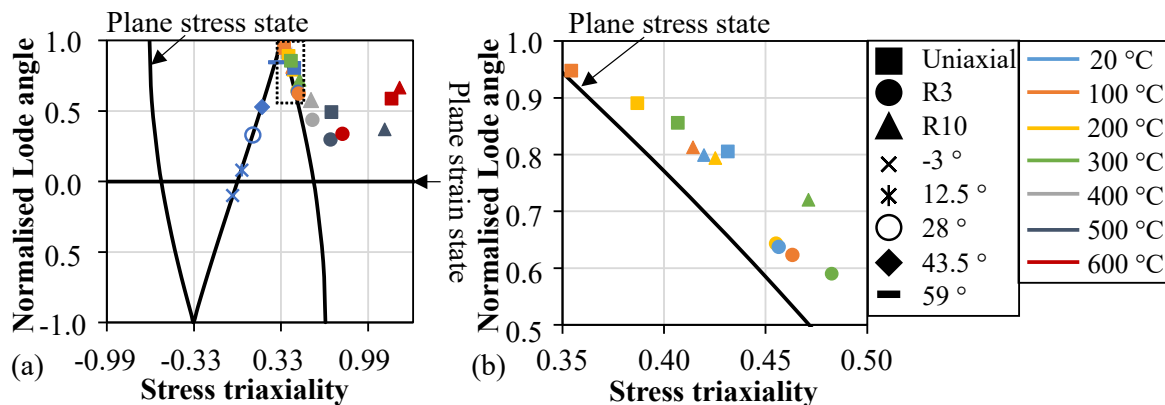


Fig. 5. Normalised Lode angle over stress triaxiality of miniaturised and butterfly tensile specimens at all temperatures at 0.001 1/s (a), a detailed illustration of $\bar{\theta}_{av}$ over η_{av} at temperatures 20 - 300 °C (b).

Similar diagrams of normalised Lode angle over stress triaxiality were generated for high speed tensile tests at 20°C. Subsequently, the abovementioned results were used to parametrise the MMC failure model and to determine the temperature and strain rate extension terms.

MMC failure surfaces. At first, the numerical results were used to parametrise c_1 , c_2 and c_3 of the MMC fracture model at 20°C and 0.001 1/s. For this purpose, the results of the tensile tests on miniaturised and butterfly specimens at 20°C and 0.001 1/s were used, specifically the ascertained

plastic strain at fracture, average stress triaxiality and average normalised Lode angle. The parameters c_1 , c_2 and c_3 were fitted to the experimental results of the miniaturised and butterfly tensile tests by the least square method. The resulting fracture surface is shown in Fig. 6 a). In Fig. 6 b), the fitted plastic strain at fracture is shown as a function of stress triaxiality in a plane stress state, together with the experimentally determined values.

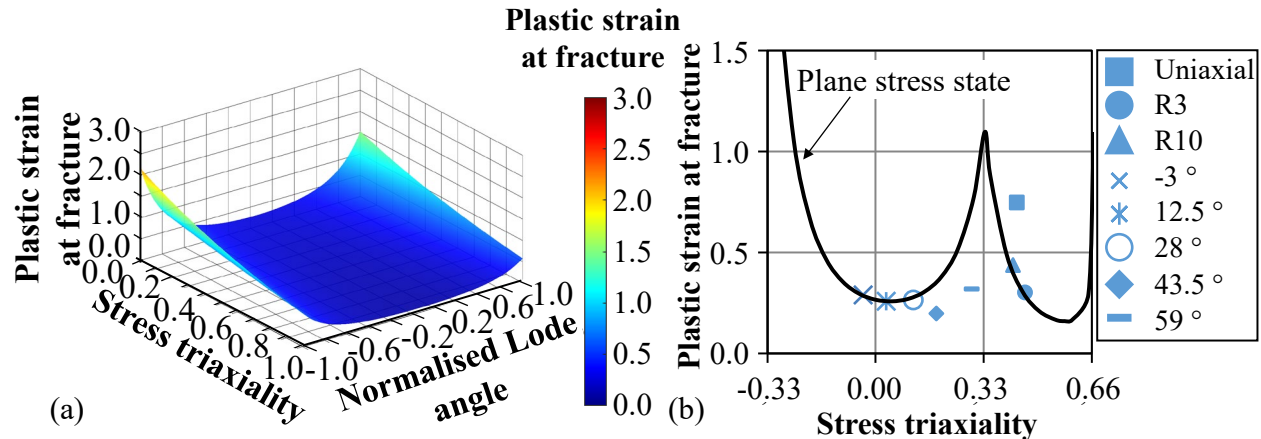


Fig. 6. MMC failure surface at 20 °C and 0.001 1/s (a), plastic strain at fracture over stress triaxiality of miniaturised and butterfly tensile tests at 20 °C and 0.001 1/s in a plane stress state (b).

Subsequently, the parametrisation of the temperature term d_1 was carried out, using the miniaturised tensile tests at various temperatures. As mentioned above, DP980 sheet material shows a non-typical steel behaviour called blue-brittleness in a temperature range of 20 - 300°C. For this reason, the parameter d_1 was determined for two different temperature fields: 20 - 300°C and 400 - 600°C, while the parameters A , n , c_1 , c_2 and c_3 were held constant. The failure surfaces of the MMC fracture model, extended by the temperature term d_1 , are shown in Fig. 7 (a) for the temperature field of 20 - 300°C and in Fig. 7 (b) for the temperature field of 400 - 600°C, both at 0.001 1/s. It can be clearly seen, that the rising temperature increases the plastic strain at fracture. Lastly, the parametrisation of the strain-rate factor d_2 was carried out using miniaturised uniaxial and high speed tensile tests at 20°C, while the parameters A , n , c_1 , c_2 , c_3 and d_1 were held constant. The acquired MMC failure surfaces of the extended equation are shown in Fig. 7 (c) for 20°C. The built failure surfaces clearly indicate, that an increasing strain rate decreases the plastic strain at fracture.

It can be therefore concluded, that it is possible to consider the strain rate and temperature dependant material behaviour by implementing the strain rate hardening and thermal softening effect terms directly in the MMC fracture model. Such parametrised equation can be furtherly used to execute numerical simulations of various sheet metal forming processes, such as shear cutting, to correctly predict material failure while taking strain rate and temperature influence into account.

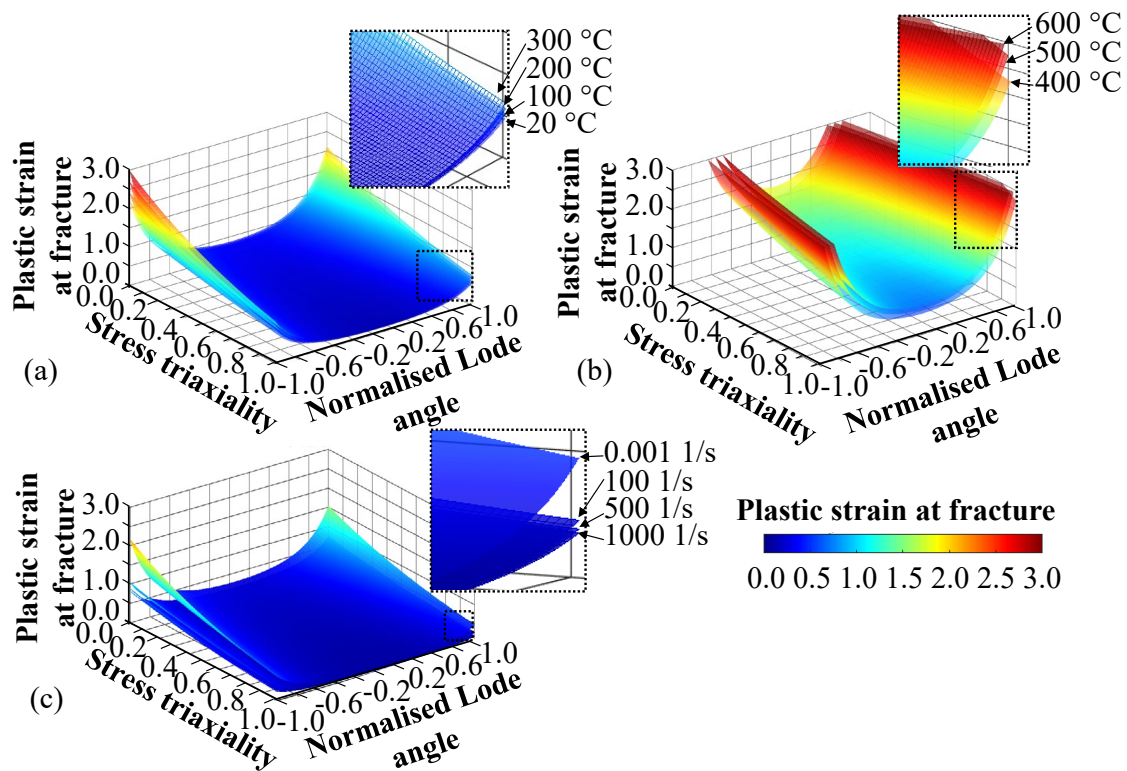


Fig. 7. Extended MMC failure surfaces of: a temperature field between 20 - 300°C at 0.001 1/s (a), a temperature field between 400 - 600°C at 0.001 1/s (b), a strain-rate field between 0.001 - 1000 1/s at 20°C (c).

The individual values of average stress triaxiality, average normalised Lode angle and plastic strain at fracture, determined numerically and used to parametrise the MMC fracture model, are listed in the following tables. Table 1 shows the values regarding temperature dependency, obtained from the miniaturised tensile test specimens of uniaxial, both notched R3 and R10 geometries at 0.001 1/s. Table 2 shows the values regarding the load angle of the butterfly tensile tests at 20°C and 0.001 1/s (left) and the high speed tensile tests at 20°C (right). Lastly, Table 3 holds the individual parameters of the extended MMC failure model.

Table 1. Temperature dependent average stress triaxiality, average normalised Lode angle and plastic strain at fracture of the miniaturised tensile test specimens of uniaxial, R3 and R10 geometries at 0.001 1/s.

Temperature in °C	Uniaxial			R3			R10		
	η_{av}	$\bar{\theta}_{av}$	$\bar{\varepsilon}_p^f$	η_{av}	$\bar{\theta}_{av}$	$\bar{\varepsilon}_p^f$	η_{av}	$\bar{\theta}_{av}$	$\bar{\varepsilon}_p^f$
20	0.43	0.81	0.75	0.46	0.64	0.30	0.42	0.79	0.44
100	0.35	0.95	0.39	0.46	0.62	0.32	0.41	0.81	0.41
200	0.36	0.89	0.57	0.46	0.64	0.31	0.42	0.79	0.48
300	0.41	0.86	0.67	0.48	0.59	0.49	0.47	0.72	0.68
400	0.37	0.91	0.36	0.57	0.44	0.67	0.56	0.58	0.84
500	0.71	0.49	1.43	0.71	0.29	1.02	1.12	0.37	1.60
600	1.17	0.59	1.81	0.79	0.34	1.70	1.23	0.67	1.89

Table 2. Average stress triaxiality, average normalised Lode angle and plastic strain at fracture of butterfly tensile tests at 20 °C and 0.001 1/s (left), and of high speed tensile tests at 20 °C (right).

Butterfly tensile tests				High speed tensile tests			
Load angle in °	η_{av}	$\overline{\theta}_{av}$	$\overline{\varepsilon}_p^f$	Strain rate 1/s	η_{av}	$\overline{\theta}_{av}$	$\overline{\varepsilon}_p^f$
-3	-0.04	-0.09	0.29	100	0.36	0.93	0.33
12.5	0.03	0.08	0.26	500	0.39	0.81	0.26
28	0.12	0.33	0.26	1000	0.33	0.99	0.06
43.5	0.19	0.53	0.19				
59	0.29	0.85	0.32				

Table 3. Parameters of the extended MMC fracture model.

c_1	c_2	c_3	A	n	d_1 (T = 20 - 300 °C)	d_1 (T = 400 - 600 °C)	d_2
0.04	760	1.005	1450	0.0775	2	15	-0.045

Summary

Due to the temperature and strain rate increase in certain industrial sheet metal processes such as shear cutting, it is essential to considerate material's dependency on aforementioned parameters in material modelling to ensure accurate simulation results. Therefore, the aim of this paper is to extend the Modified Mohr-Coulomb fracture model by a temperature and strain rate dependant term for a DP980 steel sheet. For this purpose, Johnson-Cook strain rate hardening and thermal softening effect terms were applied as extension parameters. For the variable parametrisation of the extended MMC model, experimental results from various tensile tests were used, which covered a process relevant stress, temperature and strain rate field. Subsequently, the acquired experimental tests were simulated in Abaqus/implicit to obtain the required parameters of average stress triaxiality, average normalised Lode angle and plastic strain at fracture. Finally, the results were used to determine the individual parameters of the MMC model as well as of the temperature and strain rate dependant terms, which served as an extension of the MMC failure model. In future investigations, the extended model will be applied in a shear cutting simulation and validated using experimental data, so it can be subsequently considered in the simulation of an industrial sheet metal process to improve material's failure prediction and subsequently the process design.

Acknowledgement

The authors are much obliged to the DFG (German Research Foundation) for the financial support of the project "Improved FE simulation of the shear cutting process using a temperature and strain rate-dependent extension of the MMC model" (project number: 199808648).

References

- [1] M. Schneider, I. Peshekhodov, A. Bouguecha, B.-A. Behrens, A new approach for user-independent determination of formability of a steel sheet sheared edge, *Prod. Eng.* 10 (2016) 241-252. <https://doi.org/10.1007/s11740-016-0677-4>
- [2] B.-A. Behrens, D. Rosenbusch, H. Wester, P. Althaus, Comparison of three different ductile damage models for deep drawing simulation of high-strength steels, *IOP Conf. Ser.: Mater. Sci. Eng.* 1238 (2022) 12021. <http://doi:10.1088/1757-899X/1238/1/012021>
- [3] X. Xiao, H. Pan, Y. Bai, Y. Lou, L. Chen, Application of the modified Mohr-Coulomb fracture criterion in predicting the ballistic resistance of 2024-T351 aluminum alloy plates impacted by blunt projectiles, *Int. J. Impact Eng.* 123 (2019) 26-37. <https://doi:10.1016/j.ijimpeng.2018.09.015>

- [4] G. R. Johnson, W. H. Cook, Fracture characteristics of three metals subjected to various strains, strain rates, temperatures and pressures, *Eng. Fract. Mech.* 21 (1985) 31-48. [https://doi.org/10.1016/0013-7944\(85\)90052-9](https://doi.org/10.1016/0013-7944(85)90052-9)
- [5] Y. Bai, T. Wierzbicki, Application of extended Mohr-Coulomb criterion to ductile fracture, *Int. J. Fract.* 161 (2010) 1. <https://doi.org/10.1007/s10704-009-9422-8>
- [6] B.-A. Behrens, K. Brunotte, H. Wester, C. Kock, D. Kildonaviciute, Determination of temperature dependence in Modified-Mohr-Coulomb failure model for process simulation of shear cutting, *IOP Conf. Ser.: Mater. Sci. Eng.* 1238 (2022) 12028. <http://doi.org/10.1088/1757-899X/1238/1/012028>
- [7] M. J. Mirnia, M. Shamsari, Numerical prediction of failure in single point incremental forming using a phenomenological ductile fracture criterion, *J. Mater. Process. Technol.* 244 (2017) 17-43. <https://doi.org/10.1016/j.jmatprotec.2017.01.029>
- [8] C. R. Roth, D. Mohr, Effect of strain rate on ductile fracture initiation in advanced high strength steel sheets: Experiments and modeling, *Int. J. Plast.* 56 (2014) 19-44. <https://doi.org/10.1016/j.ijplas.2014.01.003>
- [9] J. Cao, Z. Sun, L. Huang, Z. Yin, A unified model of ductile fracture considering strain rate and temperature under the complex stress states, *J. Mater. Process. Technol.* 297 (2021) 117275. <https://doi.org/10.1016/j.jmatprotec.2021.117275>
- [10] R. Indhu, S. Soundarapandian and L. Vijayaraghavan, Yb: YAG laser welding of dual phase steel to aluminium alloy, *J. Mater. Process. Technol.* 262 (2018) 411-421. <https://doi.org/10.1016/j.jmatprotec.2018.05.022>
- [11] B.-A. Behrens, K. Brunotte, H. Wester, M. Dykiert, Fracture Characterisation by Butterfly-Tests and Damage Modelling of Advanced High Strength Steels, *Key Engineering Materials* 883 (2021) 294-302. <https://doi.org/10.4028/www.scientific.net/KEM.883.294>
- [12] H. W. Swift, Plastic instability under plane stress, *J. Mech. Phys. Solids* 1 (1952) 1-18. [https://doi.org/10.1016/0022-5096\(52\)90002-1](https://doi.org/10.1016/0022-5096(52)90002-1)
- [13] E. Voce, The relationship between stress and strain for homogeneous deformations, *J. Inst. Met.* 74 (1948) 537-562
- [14] J. Qin, R. Chen, X. Wen, Y. Lin, M. Liang, F. Lu, Mechanical behaviour of dual-phase high-strength steel under high strain rate tensile loading, *Materials Science and Engineering: A* 586 (2013) 62-70. <http://doi.org/10.1016/j.msea.2013.07.091>
- [15] E. Cadoni, N. Singh, D. Forni, M. K. Singha, N. K. Gupta, Strain rate effects on the mechanical behavior of two Dual Phase steels in tension, *The European Physical Journal Special Topics* 225 (2016) 986-993. <http://doi.org/10.1140/epjst/e2016-02638-3>
- [16] F. Gutknecht, F. Steinbach, T. Hammer, T. Clausmeyer, W. Volk, A. E. Tekkaya, Analysis of shear cutting of dual phase steel by application of an advanced damage model, *Procedia Struct. Integr* 2 (2016) 1700-1707. <https://doi.org/10.1016/j.prostr.2016.06.215>